Object Motion with Structured Optical Illumination as a Basis for Far-Subwavelength Resolution

Kevin J. Webb, Yulu Chen, and Trevor A. Smith

Object motion with structured optical illumination as a basis for far-subwavelength resolution

Kevin J. Webb[1*], Yulu Chen

School of Electrical and Computer Engineering,

Purdue University, West Lafayette, IN 47907, USA

Trevor A. Smith

School of Chemistry, The University of Melbourne, Parkville, Vic 3010, Australia

[*]Corresponding author: webb@purdue.edu

Abstract

An imaging method based on object motion with structured light illumination and far-field measurement data that results in far-subwavelength image information is proposed. Simulations with realistic noisy data show that this approach will lead to the ability to distinguish object features on the nanometer scale using visible light, without the need for fluorophores. The principle is that far-field measurements with controlled motion in a spatially varying incident field add information about nanometer-scale dimensions and material properties.

PACS numbers: 41.20.Jb, 42.25.Fx, 42.30.Va, 42.30.Wb

I. INTRODUCTION

For a very long time it has been accepted that the resolution of any far-field imaging system is fundamentally limited by the wavelength of the radiation and the refractive index of the optics used. For a large numerical aperture lens, this results in a resolution proportional to $\lambda_0/(2n)$, where λ_0 is the free space wavelength and n is the refractive index. The restriction of the maximum achievable resolution to about one half of a wavelength, known as the (Abbe) diffraction limit [1], has driven the use of shorter wavelengths for lithography and optical data storage, as well as optics with larger background refractive index (immersion optics) in order to obtain improved resolution. However, in applications there are practical limits to how short the wavelength can become, motivating efforts to circumvent the link between wavelength and resolution.

The mathematical picture for the diffraction limit comes from a plane wave field expansion in the near-field and the removal of the evanescent fields, which are below the noise floor of a detector in the far-field where most optical systems operate. Use of near-field scanning methods allow measurement of the evanescent fields, but such approaches may not be practical in applications. Structured illumination and the Moiré effect provide a means to determine object information in the far-field with an improvement in resolution of up to a factor of two [2, 3]. Also, quantum imaging using a Hanbury Brown-Twiss scheme allows the Abbe limit to be overcome when imaging equi-distant sources [4, 5].

Subwavelength spatial resolution has been achieved using fluorescence microscopy [6–8]. In stimulated emission depletion (STED) microscopy, a patterned beam (such as a donut shape) is scanned along with the excitation beam, and all photoexcited fluorophores are driven to a dark state except those near the center of the point spread function. The spatial resolution is thus defined by the depleting beam, and a lateral resolution of $\lambda_0/45$ and a longitudinal resolution of about three times this have been shown [7, 9, 10]. This approach was limited by the need for reversible photophysical behavior of the fluorophore. In photoactivated localization microscopy (PALM) [8], and in stochastic optical reconstruction microscopy (STORM) [11], a subset of molecules are activated, and it is assumed that the distance between any two of these emitters is greater than $\lambda_0/(2n)$. The emitter can then be localized to a precision limited by the determination of the emission peak in space at the detector. Three-dimensional imaging has been facilitated by design of the point spread

function of the imaging system [12, 13]. While used with great success, these forms of microscopy are limited by the need to introduce (sometimes specific) fluorescent molecules or nanoparticles, a situation that may not always be possible in practice.

Another approach to increase resolution is to modify the lens design so that information about the subwavelength features, contained in the evanescent fields, is retained. The ideal negative refractive index lens can in principle retain all evanescent field information [14, 15], but without magnification. However, loss and mismatched material parameters have a dramatic impact on the evanescent field transfer function and hence the attainable resolution [16–18]. While a recent operating arrangement of the material parameters offers promise [19], foreseeable offset distances remain small. Layered materials having alternating regions of metal and dielectric, can yield a homogenized material response with hyperbolic dispersion that allows the transfer of TM-polarized evanescent fields across the material [20–23]. The evanescent fields of course decay quickly either side of the material, again limiting the offset distance. By introducing curvature into the lens, subwavelength features can be imaged to the far-field [24, 25], and a design space exists for applications [26, 27]. A TM surface standing wave at a metal-insulator interface (a surface plasmon standing wave) has been proposed for enhanced resolution with structured illumination [28]. Use of structured illumination in a hyperbolic material, with a resolution related to the spatial variation of the illumination field, has also been suggested [29]. Both of these approaches rely on the object being in close proximity to the surface/material.

We present a new approach for retrieving subwavelength object information that does not use special lens materials and requires neither the introduction of a fluorophore nor the assumption of spatially disparate elements - separated by more than $\lambda_0/(2n)$. By employing a structured incident field and then performing a set of far-field measurements using detector arrays as a function of scanned object position, we show using simulated noisy data that $\lambda_0/100$ resolution can readily be achieved with substantial detector noise. This is possible because of the additional information on the object's location in a structured field that varies on the wavelength scale, achievable in an experiment with an available source, positioner and photodetector. Unlike near-field scanning methods that access small collection volumes and are restricted to surface information, our approach of scanning the object position with far-field measurements allows scattered light from the whole object to be measured at each of the object positions.

II. ILLUSTRATING CONCEPT

We consider a 2D simulation geometry where two small square scatterers (with dielectric constant $\epsilon_r = 1.5$) are moved around in a free space background, as shown in Fig. 1(a). The numerical finite element method (FEM - COMSOL) simulation used an incident field wavelength of $\lambda = 1$ μm, but the problem is scalable, and all data as a function of spatial coordinates are presented in terms of wavelength. The size of the free space background is 6λ by 6λ, and it is surrounded by 2λ-thick perfectly matched layers (PML) on all sides to simulate unbounded space. The square scatterers are of dimension 0.05λ, and their edge-to-edge separation is denoted by D, as shown in Fig. 1(b). The two scatterers with fixed relative positions are scanned in both the $\hat{\mathbf{x}}$- and $\hat{\mathbf{y}}$-directions with a step size of 0.1λ over a region of λ by λ (denoted by the blue square in the center of Fig. 1(a)).

We use two illumination schemes. The first (PW) is a single plane wave with $\mathbf{E}$ in the $\hat{\mathbf{z}}$-direction and incident from the left, hence propagating in the $\hat{\mathbf{x}}$-direction (assuming $\exp(-i\omega t)$ dependence) as

$$\mathbf{E} = \sqrt{2}e^{ikx}\hat{\mathbf{z}}, \tag{1}$$

where $k = 2\pi/\lambda$. The second scheme (SI for structured illumination) is the superposition of two plane waves, both having $\mathbf{E}$ in the $\hat{\mathbf{z}}$-direction, one propagating in the $\hat{\mathbf{x}}$-direction and the other in the $\hat{\mathbf{y}}$-direction, giving

$$\mathbf{E} = (e^{ikx} + e^{iky})\hat{\mathbf{z}}. \tag{2}$$

Two detector arrays, s_1 and s_2, are used to measure power in the transmission direction and are shown as the red dotted lines in Fig. 1(a). Both s_1 and s_2 are 0.5 λ from the PML boundaries, and the length of each is 5 λ.

For the PW case, we use s_2 to measure the time-averaged Poynting vector in the $\hat{\mathbf{x}}$-direction, S_x. For a single plane wave described by (1), $S_x = 1/\eta$, where η is the (free space) wave impedance. The total power detected by s_2 without the object is $P_{\mathrm{PW}} = 5\lambda/\eta$. For the SI case, s_1 is also used to measure the time-averaged Poynting vector in the $\hat{\mathbf{y}}$-direction, S_y. From (2), $S_x = S_y = [1 + \cos(kx - ky)]/(2\eta)$. Therefore, the total power into s_1 and s_2 is $P_{\mathrm{SI}} = 5\lambda/\eta$, identical to the PW case when there is no object present. This arrangement of equal detected powers for both cases provides a basis for comparison.

In the FEM simulations, a mesh was generated at each scanned object position that had a maximum size of 0.02λ, and the minimum mesh size was 0.001λ. There were at

4

least 8 layers of mesh elements between the two scatterers. When the maximum mesh was reduced to 0.01λ, the change in the Poynting vector information was 6 orders of magnitude smaller. Our investigation of numerical precision led us to conclude that the field solution and simulated detected power data are sufficiently accurate for our purpose.

III.   DETECTOR NOISE MODEL

We choose a signal-to-noise ratio (SNR) of 40 dB to establish error bars in 2D simulations of power density, and a simple argument for a 3D experiment provides a basis. The detector signal-to-noise ratio is SNR $= \langle I \rangle^2 / \sigma_I^2$, where $\langle I \rangle$ is the average photodetector current and σ_I^2 is the variance. We assume that at each detector the additive (current) noise is a zero-mean Gaussian random variable whose standard deviation is proportional to the detected time-averaged Poynting vector. The noise equivalent power (NEP W/$\sqrt{\text{Hz}}$) is the optical signal power needed to make the electrical SNR=1 in a $B = 1$ Hz bandwidth. Writing $\sigma_I^2 = 2e\langle I_n \rangle B$ for detector integration time $T = (2B)^{-1}$, with $\langle I_n \rangle$ the average noise current (so $I_n = I$ gives Poisson-based shot noise) and e the magnitude of the electron charge, $\langle I \rangle = \kappa \, \text{NEP} = \sigma_I = \sqrt{2e\langle I_n \rangle}$, where κ (A/W) is the photodetector responsivity. Consider the thermal noise limit, and a dark current count rate of R electrons/s, resulting in NEP $= (e/\kappa)\sqrt{2R}$. We define a Poynting vector SNR $= S_d / \sigma_s$, where S_d is the Poynting vector magnitude (mean) at the detector and σ_s is the standard deviation, a reflection of the detector noise. Setting $\sigma_s = \text{NEP}/A_e$, with A_e the effective detector aperture, gives a measure of detector noise. A typical NEP range for commercially available avalanche photodiodes (APDs) and photomultiplier tubes is $10^{-18} - 10^{-17}$ W/$\sqrt{\text{Hz}}$, and 10^{-22} W/$\sqrt{\text{Hz}}$ has been achieved for single-photon-counting detection with an APD operated at 78 K [30]. A convenient laser source and detector size suggests the 40 dB SNR value we employ in our 2D simulations is conservative.

IV.   RESULTS

In Fig. 2, we plot S_x information measured along s_2 (Fig. 1(a)) for both the PW and SI cases when the (two $\epsilon_r = 1.5$) scatterers are at reference position $(0,0)$ for three different values of separation, D. In Figs. 2(b) and (d), we show differences between the detector

measurements for the three scatterer separations, using the $D = 0.02\,\lambda$ case as a reference. Because of the relatively weak scatter, the measured data in Figs. 2(a) and (c) for the PW and SI cases, respectively, is very close to that for the incident field alone. Figures 2(b) and (d) show error bars determined from a 40 dB SNR, resulting in $\sigma_s = S_d/\mathrm{SNR} = 10^{-4} S_d$. The end-to-end length of the error bars is equal to twice the standard deviation of the noise process. As expected, the 0.01λ change in D cannot be resolved by detectors having a 40 dB SNR.

We use $(\Delta x, \Delta y)$ to represent the shift from the central, reference position of the two scatterers, $(0,0)$. As the scatterers are scanned while preserving the geometry, the time-averaged Poynting vector measured at the detectors is compared with the Poynting vector data with the object at the reference position. Consider then the function

$$f(\Delta x, \Delta y; D) = \int [\mathbf{S}(x, y; \Delta x, \Delta y, D) - \mathbf{S}(x, y; 0, 0, D)] \cdot d\mathbf{s}, \tag{3}$$

which is the integral of the change in detected power due to motion over a surface (line in our case) defined by $\mathbf{s}$ with a fixed scatterer separation, D. For the PW case, $\mathbf{s}$ includes only s_2, while for SI, $\mathbf{s}$ contains both s_1 $(d\mathbf{s} = \hat{\mathbf{y}} dx dz \to \hat{\mathbf{y}} dx)$ and s_2 $(d\mathbf{s} = \hat{\mathbf{x}} dy dz \to \hat{\mathbf{x}} dy)$. When noise is incorporated into the data, $f \to f_n$ in (3), so that it becomes

$$f_n(\Delta x, \Delta y; D) = \int [\mathbf{S}_n(x, y; \Delta x, \Delta y, D) - \mathbf{S}_n(x, y; 0, 0, D)] \cdot d\mathbf{s}, \tag{4}$$

where $\mathbf{S}_n$ is the Poynting vector data with noise added. Because the ranges of f and f_n are much greater than the small differences induced by the far-subwavelength change in D, we introduce

$$g(\Delta x, \Delta y; D) = f_n(\Delta x, \Delta y; D) - f(\Delta x, \Delta y; D_0), \tag{5}$$

which reflects the change in D and in the detector data due to the motion of scatterers. Figure 3 shows $g(\Delta x, \Delta y; D)$ when the scatterers are scanned along the bottom $(\Delta y = -0.5\lambda)$ and left $(\Delta x = -0.5\lambda)$ boundaries, referring to Fig. 1, for $D_0 = 0.02\lambda$ and both the PW and SI cases. The error bars in Fig. 3 were obtained by adding noise to the Poynting vector 100 times and calculating the standard deviation of the resulting f_n and g. In Figs. 3(a) and (b), we see that the 0.01λ change in D is barely resolvable in $g(\Delta x, \Delta y; D)$ with a single incident plane wave and a 40 dB SNR. However, Figs. 3(c) and (d) show that the 0.01λ change in D can be easily resolved for the SI case. This resolution enhancement is due to the additional information encoded into the far-field scattered field (represented

in the change in S_x and S_y) by the interaction between the scatterers and the structured illumination.

Based on the sensitivity that has now been established, we propose a method to determine the far-subwavelength distance between two scatterers as well as their dielectric constants. We use the notation $f(\Delta x, \Delta y; D, \epsilon_r)$ with an unknown dielectric constant for the scatterers. An experiment will yield $f_n(\Delta x, \Delta y; D, \epsilon_r)$ from far-field power measurements. Determination of the correct values of D and ϵ_r, denoted by D^* and ϵ_r^*, from the forward calculation of $f(\Delta x, \Delta y; D, \epsilon_r)$ for possible values of D and ϵ_r is achieved by minimizing the cost function

$$(D^*, \epsilon_r^*) = \underset{\{D, \epsilon_r\}}{\operatorname{argmin}} \sum_{\Delta x, \Delta y} |f_n(\Delta x, \Delta y; D, \epsilon_r) - f(\Delta x, \Delta y; D, \epsilon_r)|. \tag{6}$$

Figure 4 shows results from (6) for a hypothetical experiment with $D^* = 0.02\lambda$ and $\epsilon_r^* = 1.5$ for the PW (Fig. 4(a)) and SI (Fig. 4(b)) cases. The scatterers were scanned over a region of 0.5λ by 0.5λ to save computation time. Note that the minimum cost is with the correct separation and dielectric constant, despite the rather large SNR of 40 dB. We plot the cost at the correct ϵ_r as a function of D for the PW and SI cases in Figs. 4(c) and (d), respectively, in order to show the influence of detector noise in relation to the cost function features - as (barely noticeable) error bars. The error bars in Figs. 4(c) and (d) were obtained numerically by randomly choosing noisy Poynting vector data and calculating the resulting standard deviation in the cost function. Notice that there is less sensitivity in the cost to variations in D for the PW case relative to that with SI. This is in agreement with the data presented in Figs. 3(a) and (b) (PW) relative to Figs. 3(c) and (d) (SI). Figure 5 shows results from another hypothetical experiment with $D^* = 0$ (a single scatterer) and $\epsilon_r^* = 2.5$, with 40 dB SNR error bars determined numerically. The method clearly works with $D^* = 0$, meaning that it is possible to distinguish one large scatterer from two smaller scatterers.

We also demonstrate that it is possible to determine differing dielectric constants within an object. Assuming that the dielectric constants of the two scatterers can be any value among 1.2, 1.4, 1.6, 1.8, and 2, the calculated cost functions in Fig. 6(a) show that the cost is minimized at the correct values, $\epsilon_{r1}^* = 1.4$ and $\epsilon_{r2}^* = 1.6$. Figures 6(b) and (c) give the cost evaluated as a function of each variable, along with the relatively small uncertainty error bars associated with detector noise. Note that this example shows sensitivity to weak scatter and to small differences in the dielectric constant.

V. DISCUSSION AND APPLICATIONS

Far-field detector data as a function of scanned, known object position in a spatially varying field provides information about far-subwavelength object features. The principle is that a non-deformable object is positioned at a set of points with step size small relative to the optical wavelength. The object should be scanned through at least one wavelength in each relevant dimension. Physically, the scattered field dipole moment varies with position in the structured incident field, and this gives rise to the variation in detected data. Information is added because of the known object positions, and knowledge of a reference result, without the object or with the object at a particular location. That location does not need to be known precisely, but the scan steps from this reference position must be known. For our example in Fig. 1, this scan involves translating the object (with fixed arrangement, including particle orientation and separation) over a Cartesian grid within the blue region (λ on a side). The evidence presented is for classification, whereby a decision can be made which of a set of possible results for different objects best fits the measurement. This corresponds to use of prior measurement information or a prediction. We show an ability to determine small changes (in geometry). This is equivalent to sensitivity to the differential change in geometry. While the object we considered was small relative to the wavelength, there should in principle be no restriction on the object size, although there will be practical limits dictated by the instrument. From a practical perspective, the size of the object may impact the detected signal (and hence the detector shot noise).

Our results in Figs. 3, 4, and 5 show that far-field measurements of power as a function of object position in a structured field provide information about feature size on the scale of 0.01λ. To the contrary, and as is well known, Fig. 2 shows that this information is not available with a stationary object. The reason for this resolution enhancement is that improved sensitivity results from spatial diversity, both in terms of known object location and known multiple detector locations. This increases the SNR, for a fixed detector noise (or integration time), and does so for structured (Figs. 3(c) and (d)) over unstructured (Figs. 3(a) and (b)) illumination. Notice that both the mean and the error in estimating the mean (the noise or error bars) are smaller in Figs. 3(c) and (d) relative to Figs. 3(a) and (b). Also, simply moving the objects in a plane wave field with fixed detectors (Figs. 3(a) and (b)) provides some improvement over that possible with fixed object position (Fig. 2).

8

This occurred for two reasons, one being the benefit of motion with fixed illumination and detectors, and the other the fact that the data in Fig. 3 is integrated over detector position, through the definition of g in (5), which increases the SNR.

The computational domain and the detector location (Fig. 1) involved a convenient trade-off for the simulations. We wanted to ensure measurements in the far-field, so that the evanescent fields were negligible, but preserve a reasonably small computational domain to achieve a manageable and simple and highly accurate set of simulations. The propagating waves are detected, so in principle the detectors could be at any distance from the objects. There will of course be practical limits. However, as the detector plane moves away from the object, the size of the measurement surface needs to be increased to capture equivalent information, but the sample density could be reduced. In reality, a lens or a fiber-based collection system would be used in implementation.

Our approach requires scanning the object, so enhanced spatial resolution comes at this price. However, near-field scanning optical microscopy also requires the sample to be moved, but in addition the aperture may interfere with the light scattered by the object, and that method suffers from substantial light attenuation through the tapered fiber. Our approach allows far-field light collection, is simpler and offers higher signal level. Scanning an object in a field is reminiscent of ptychography experiments, where image information has been enhanced primarily by achieving a synthetic aperture effect with a diffuser to broaden the spatial frequency content of the illuminating probe [31]. However, our goal of achieving subwavelength image information and approach differ significantly from this.

Consider now how an experiment could be conducted and how the feature identification, for example, the distance between two objects of assumed size and material, could be determined. Measurement with an array of detectors allows $f_n(\Delta x, \Delta y)$, the noisy data corresponding to (3), to be determined. The reference result is with the object at the position $\Delta x = 0, \Delta y = 0$. This leads directly to the type of data we presented in normalized form in Fig. 3. The structured field could in principle have any character. Three or more laser beams would provide suitable illumination for three-dimensional imaging. The structured illumination could be periodic, as we considered, or of some other form, such as speckle [32]. The issue is how to use this data to determine the spacing between the two elements of the object, D. Simplistically, this could be achieved by making the same set of measurements with known and different D. Comparison with the unknown object data would allow se-

9

lection of the best candidate. A more sophisticated approach is to determine the nature of the structured field using measurements without the object, and then form a model for the scattered field due to the object. This is what we did in the numerical studies. In this way, predicted measurements could be compared with the actual data to determine D. This latter approach relates to the more general computational imaging problem.

Precise spatial scanning of the object is possible with piezoelectric stages that are routinely used in atomic force microscopy. Given wavelength-scale structure in the field, and the possible stage motion and detector noise, it appears that a spatial resolution on the order of 1 nm might be achievable with visible light. Scanning with a piezoelectric stage and making measurements at each position can be effective in nanostructured solid-state material applications. However, imaging dynamic systems such as live biological cells will be more challenging. In principle, all that is needed is to scan faster. However, the number of positions needed may preclude the use of a piezoelectric stage for adjustment of the the object position. It may be possible to modify the imaging concept we present along the following lines. A mechanical wave could move a biological cell system, and perhaps by careful calibration it might be possible to determine the change in position of the sample. For instance, an acoustic pressure wave applied in three orthogonal directions might allow this, assuming that the time-gating applied to the optical measurement is fast relative to this motion (or that this can be de-convolved). Another approach could be to use an optical beam to apply a force to move the sample. Motion of cells could be achieved directly with a laser. For example, a laser beam has been shown to deform the surface of water due to the optical force [33]. While current optical tweezer technology uses beads and relatively high power laser beams [34, 35], possibly an issue for biological cells, there may be compromise ground that is suitable for live cells.

We considered the questions of determining whether there were one or two objects, the far-subwavelength distance between the objects, and their dielectric constant. For instance, a question might be to determine the separation between two objects. This type of classification method amounts to a set of constraints that simplifies an imaging problem to one of classification. More general computational imaging would involve a cost function imaging method [36]. In principle, the image domain could be tiled as pixels (voxels in three dimensions), with the material properties in each voxel constant. This would be equivalent to a discrete, finite difference, basis set, and that grid could be 0.01 λ, for example. The

cost function approach would minimize the difference between the measured data, with the object at a series of positions, and the results from calculations that seek to predict the measurement. In this way, complete images with high resolution could in principle be achieved. It may be useful to consider other spatial basis sets, and also variable domain resolution, as in multigrid, which can not only speed optimization-based solutions but also help with the quality [37]. The question of what resolution may be possible is a practical issue that will depend on variables such as positioning accuracy, detector noise, computational effort, and object contrast. There are therefore a set of experimental and computational aspects to explore with regard to general imaging utility.

The Abbe resolution limit essentially describes a spot size based on loss of evanescent field information. A key measure in resolution is the distance between two points in the object that can be resolved, and Rayleigh presented a criterion [38]. Resolution can be enhanced by deceasing the wavelength, but this is not always convenient and has practical limits. Entangled photons provide a means to increase resolution to $\lambda/(2N)$, for N entangled photons, i.e., according to the the total energy of the photons in mixed state [39], but requires an appropriate detection method. Constraints imposed in sensing or forming images have important consequences with regard to resolution. With a photon correlation of order N equal to the number of uniformly separated sources, a resolution proportional to $\lambda/(N-1)$ has been shown [5]. Furthermore, by enforcing the size of an aperture in an iterative ('sparsity-based') reconstruction scheme, a resolution beyond the measured spatial frequency information has been shown [40]. In Fig. 2, we show that the noise and data set preclude distinguishing the three different stationary objects, two small objects having center-to-center (phase center) separations of $0.06 - 0.08$ λ. This indicates constraints such as those used in the sparsity-based image reconstruction scheme will not be effective [40]. Ultimately, while Heisenberg uncertainty poses fundamental limits on measurement accuracy, practical issues limit measurements. Noise could be reduced with squeezed states [41], but reaching the resolution we suggest through detection method noise reduction will certainly be a challenge. Improvements in accuracy have been reviewed [42], and our approach provides another dimension. The key point of our work is that translating the object in a structured field adds information, as is clear from the data in Fig. 3, making the identification of the small object separation (center-to-center and edge-to-edge) and the dielectric constant (Figs. 4 and 5) possible.

Consider the situation of 0.01 λ resolution, that we suggest is readily achievable, and a plane wave decomposition of the scattered field from a stationary sample in the free space region where detection occurs. At the closest points in the scan arrangement of Fig. 1, the detectors are about 2 wavelengths from the objects. The wave expansion for a detector plane at some position along the x-axis involves a spatial variation $\exp(ik_x x)$ and a Fourier variable k_y. The two-dimensional wave equation dictates $k_x = k\sqrt{1 - (k_y/k)^2}$, with k the free space wave number, preserving the notation used in (1) and (2). Propagating waves that can be detected in the far-field have $k_y/k < 1$, and the remainder of the spectrum, with $k_y/k > 1$, describes the evanescent fields. Resolving 0.01 λ amounts to a transverse spatial frequency for the evanescent field of $k_y/k = 100$, giving $k_x \approx i100k$. The field decay of this spatial frequency after 2λ is then $\exp(ik_x 2\lambda) \approx \exp(-400\pi)$. The data in Fig. 2 show that such resolution information is not available with a stationary object and far-field measurements. The point of this paper is to indicate that with far-field measurements as a function of position in a spatially varying field, resolution at this length scale (0.01 λ) becomes possible.

A simple one-dimensional situation is a slab moving in an incident field composed of two counter-propagating plane waves, where the goal may be to find the slab thickness and dielectric constant. By moving the slab through a structured field, the scattered field dipole moment within the object is changing in a specific manner that contributes to the information content at the detectors. Using measured data as a function of scan position, a cost function could be formed that relates a model (the predicted measurement with a specific set of variables assumed - the slab thickness and dielectric constant) to the measured data, as a function of scan position. In this way, the free variables could be determined using an inversion method.

Finally, we propose an immediate application of our imaging method. The determination of the presence of defects in the semiconductor industry is challenging. In this situation, the object might consist of multiple material layers, each quite well characterized. The key question with wafer inspection is whether there is a defect or a set of defects or not. In this situation, obtaining prior measurements data or predicting the measurement with a forward model can be reasonably straight forward. The ability to find such a defect is a function of the contrast and the thickness, in relation to the detector noise. In a practical situation, the depth and lateral position of a three-dimensional defect could be determined

by scanning the water in a structured field. Our indication of the level of information available about nanostructured materials from such a measurement suggests that this is an important application domain.

VI.   CONCLUSION

The role of this paper is to introduce a new far-field far-subwavelength imaging modality, based on motion in a structured incident field, and to motivate experimental work along these lines. The proposed measurement scheme involves the precise motion of the object through a spatially varying field and the collection of far-field data at a detector array as a function of object position. Our work has shown that useful information about the object becomes available that can allow the identification of far-subwavelength length scale information, specifically, the geometry and material properties, that would otherwise be impossible to determine because of detector noise. The sensitivity of the measurement data to subwavelength scale object features is related to the structure of the incident field. The object could be a nanoparticle or collection of nanoparticles, a solid state material to be characterized, as one might consider in a more restrictive sense in ellipsometry or semiconductor wafer inspection, or a cell or biomolecule. In the case of a live cell, a suitably fast spatial scanning method would be required. In all of these applications, determining structural and material properties on the nanometer scale using light of a specified wavelength is a critical need.

VII.   ACKNOWLEDGMENT

[1] E. Abbe, "Beiträge zur theorie des mikroskops und der mikroskopischen wahrnehmung," Arch. Mikr. Anat. **9**, 413–418 (1873).

[2] R. Heintzmann and C. G. Cremer, "Laterally modulated excitation microscopy: improvement of resolution by using a diffraction grating," Proc. SPIE **3568**, 185–196 (1999).

[3] M. G. L. Gustafsson, "Surpassing the lateral resolution limit by a factor of two using structured illumination microscopy," J. Microsc. **198**, 82–87 (2000).

[4] C. Thiel, T. Bastin, J. Martin, E. Solano, J. von Zanthier, and G. S. Agarwal, "Quantum imaging with incoherent photons," Phys. Rev. Lett. **99**, 133603 (2007).

[5] S. Oppel, T. Büttner, P. Kok, and J. von Zanthier, "Superresolving multiphoton interferences with independent light sources," Phys. Rev. Lett. **109**, 233603 (2012).

[6] S. W. Hell and J. Wichmann, "Breaking the diffraction resolution limit by stimulated emission: stimulated-emission-depletion fluorescence microscopy," Opt. Lett. **19**, 780–782 (1994).

[7] S. W. Hell, "Far-field optical nanoscopy," Science **316**, 1153–1158 (2007).

[8] E. Betzig, G. H. Patterson, R. Sougrat, O. Wolf Lindwasser, S. Olenych, J. S. Bonifacino, M. W. Davidson, J. Lippincott-Schwartz, and H. F. Hess, "Imaging intracellular fluorescent proteins at nanometer resolution," Science **313**, 1642–1645 (2006).

[9] H. Blom, D. RöNnlund, L. Scott, Z. Spicarova, V. Rantanen, J. Widengren, A. Aperia, and H. Brismar, "Nearest neighbor analysis of dopamine d1 receptors and Na+-K+-ATPases in dendritic spines dissected by sted microscopy," Microscopy Research and Technique **75**, 220–228 (2012).

[10] H. Blom and J. Widengren, "{STED} microscopy - towards broadened use and scope of applications," Current Opinion in Chemical Biology **20**, 127 – 133 (2014), molecular imaging.

[11] M. J. Rust, M. Bates, and X. Zhuang, "Sub-diffraction-limit imaging by stochastic optical reconstruction microscopy (storm)," Nat. Methods **3**, 793–796 (2006).

[12] S. R. P. Pavani, M. A. Thompson, J. S. Biteen, S. J. Lord, N. Liu, R. J. Twieg, R. Piestun, and W. E. Moerner, "Three-dimensional, single-molecule fluorescence imaging beyond the diffraction limit by using a double-helix point spread function," Proc. Natl. Acad. Sci. **106**, 2995–2999 (2009), http://www.pnas.org/content/106/9/2995.full.pdf.

[13] S. Quirin, S. R. P. Pavani, and R. Piestun, "Optimal 3d single-molecule localization for superresolution microscopy with aberrations and engineered point spread functions," Proc. Natl. Acad. Sci. **109**, 675–679 (2012), http://www.pnas.org/content/109/3/675.full.pdf.

[14] J. B. Pendry, "Negative refractive index makes a perfect lens," Phys. Rev. Lett. **85**, 3966–3969 (2000).

[15] R. A. Shelby, D. R. Smith, and S. Schultz, "Experimental verification of a negative index of refraction," Science **292**, 77–79 (2001), http://science.sciencemag.org/content/292/5514/77.full.pdf.

[16] K. J. Webb, M. Yang, D. W. Ward, and K. A. Nelson, "Metrics for negative-refractive-index materials," Phys. Rev. E **70**, 035602 (2004).

[17] V. A. Podolskiy and E. E. Narimanov, "Near-sighted superlens," Opt. Lett. **30**, 75–77 (2005).

[18] M. Yang and K. J. Webb, "Poynting vector analysis of a superlens," Opt. Lett. **30**, 2382–2384 (2005).

[19] Y. Chen, Y.-C. Hsueh, M. Man, and K. J. Webb, "Enhanced and tunable resolution from an imperfect negative refractive index lens," J. Opt. Soc. Am. B **33**, 445–451 (2016).

[20] E. Shamonina, V. A. Kalinin, K. H. Ringhofer, and L. Solymar, "Imaging, compression and Poynting vector streamlines for negative permittivity materials," Electron. Lett. **37**, 1243–1244 (2001).

[21] S. A. Ramakrishna, J. B. Pendry, M. C. K. Wiltshire, and W. J. Stewart, "Imaging the near field," J. Mod. Opt. **50**, 1419–1430 (2003).

[22] K. J. Webb and M. Yang, "Subwavelength imaging with a multilayer silver film structure," Opt. Lett. **31**, 2130–2132 (2006).

[23] H. Liu, Shivanand, and K. J. Webb, "Subwavelength imaging with nonmagnetic anisotropic bilayers," Opt. Lett. **34**, 2243–2245 (2009).

[24] Z. Jacob, L. V. Alekseyev, and E. E. Narimanov, "Optical hyperlens: far-field imaging beyond the diffraction limit," Opt. Express **14**, 8247–8256 (2006).

[25] A. V. Kildishev and E. E. Narimanov, "Impedance-matched hyperlens," Opt. Lett. **32**, 3432–3434 (2007).

[26] H. Liu and K. J. Webb, "Resonance cone formation in a curved cylindrically anisotropic metamaterial film," Opt. Lett. **36**, 343–345 (2011).

[27] H. Liu and K. J. Webb, "Resonance cones in cylindrically anisotropic metamaterials: a green's function analysis," Opt. Lett. **36**, 379–381 (2011).

[28] A. I Fernndez-Domínguez, Z. Liu, and J. B Pendry, "Coherent four-fold super-resolution imaging with composite photonic–plasmonic structured illumination," ACS Photonics **2**, 341–348 (2015).

[29] E. E Narimanov, "Hyper-structured illumination." ACS Photonics (2016).

[30] M. Akiba, K. Tsujino, and M. Sasaki, "Ultrahigh-sensitivity single-photon detection with linear-mode silicon avalanche photodiode," Opt. Lett. **35**, 2621–2623 (2010).

[31] A M Maiden, M J Humphry, F Zhang, and J M Rodenburg, "Superresolution imaging via ptychography." J. Opt. Soc. Am. A, **28**, 604–612 (2011).

[32] J. A. Newman, Q. Luo, and K. J. Webb, "Imaging hidden objects with spatial speckle intensity correlations over object position," Phys. Rev. Lett. **116**, 073902 (2016).

[33] A. Ashkin and J. M. Dziedzic, "Radiation pressure on a free liquid surface," Phys. Rev. Lett. **30**, 139–142 (1973).

[34] S. F. Nrrelykke and H. Flyvbjerg, "Power spectrum analysis with least-squares fitting: Amplitude bias and its elimination, with application to optical tweezers and atomic force microscope cantilevers," Review of Scientific Instruments **81**, 075103 (2010).

[35] A. Mashaghi, P. J. Vach, and S. J. Tans, "Noise reduction by signal combination in fourier space applied to drift correction in optical tweezers," Review of Scientific Instruments **82**, 115103 (2011).

[36] A. B. Milstein, S. Oh, J. S. Reynolds, K. J. Webb, C. A. Bouman, and R. P. Millane, "Three-dimensional Bayesian optical diffusion tomography with experimental data," Opt. Lett. **27**, 95–97 (2002).

[37] S. Oh, A. B. Milstein, C. A. Bouman, and K. J. Webb, "A general framework for nonyinear multigrid inversion," IEEE Transactions on Image Processing **14**, 125–140 (2005).

[38] M. Born and E. Wolf, *Principles of Optics* (Cambridge University Press, 1999).

[39] A. N. Boto, P. Kok, D. S. Abrams, S. L. Braunstein, C. P. Williams, and J. P. Dowling, "Quantum interferometric optical lithography: Exploiting entanglement to beat the diffraction limit," Phys. Rev. Lett. **85**, 2733–2736 (2000).

[40] A. Szameit, Y. Shechtman, E. Osherovich, E. Bullkich, P. Sidorenko, H. Dana, S. Steiner, E. B. Kley, S. Gazit, T. Cohen-Hyams, S. Shoham, M. Zibulevsky, I. Yavneh, Y. C. Eldar, O. Cohen, and M. Segev, "Sparsity-based single-shot subwavelength coherent diffractive imaging," Nat. Mater. **11**, 455–459 (2012).

[41] P. Meystre and M. Sargent III, *Elements of Quantum Optics* (Springer, 1999).

[42] V. Giovannetti, S. Lloyd, and L. Maccone, "Quantum-enhanced measurements: beating the standard quantum limit," Science **306**, 1330–1336 (2004).

FIGURES

(a)   (b)
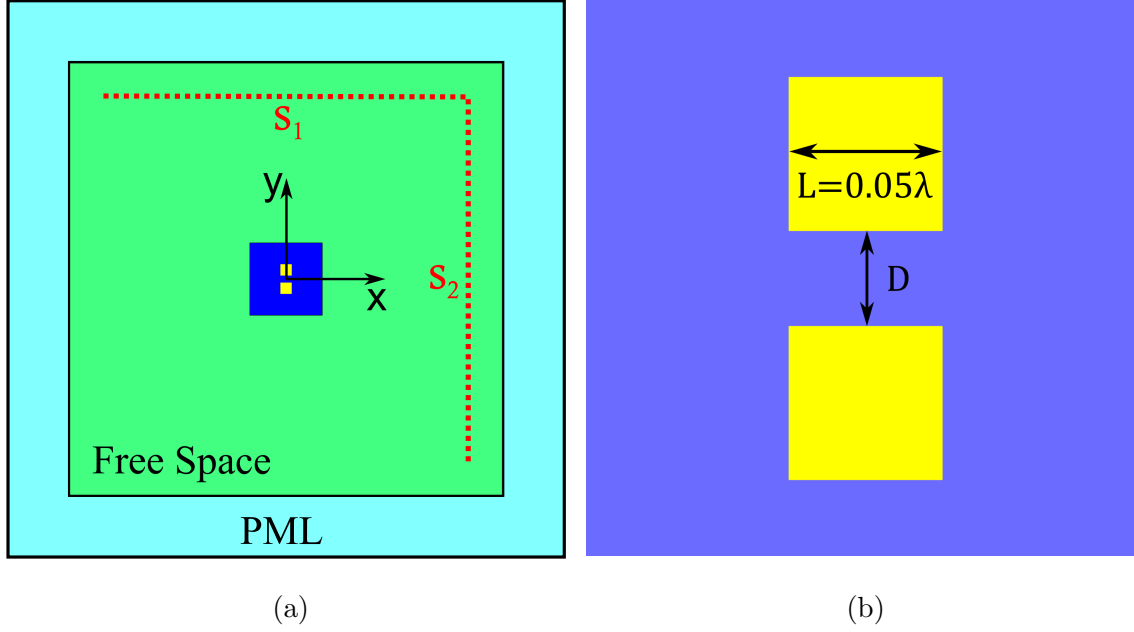
FIG. 1. (a) The square 6λ simulation geometry consists of two square scatterers ($\epsilon_r = 1.5$) scanned in 0.1λ steps in 2D. The range of motion is represented by the blue square ($1\lambda \times 1\lambda$) at the center of the free space background. The red dotted lines denote the locations of the detectors ($0.5\ \lambda$ from the PML boundaries and about $2\ \lambda$ from the objects at the closest points). (b) The central scanned region is drawn to explicitly show the dimension and arrangement of the scatterers. These figures are not drawn to scale.
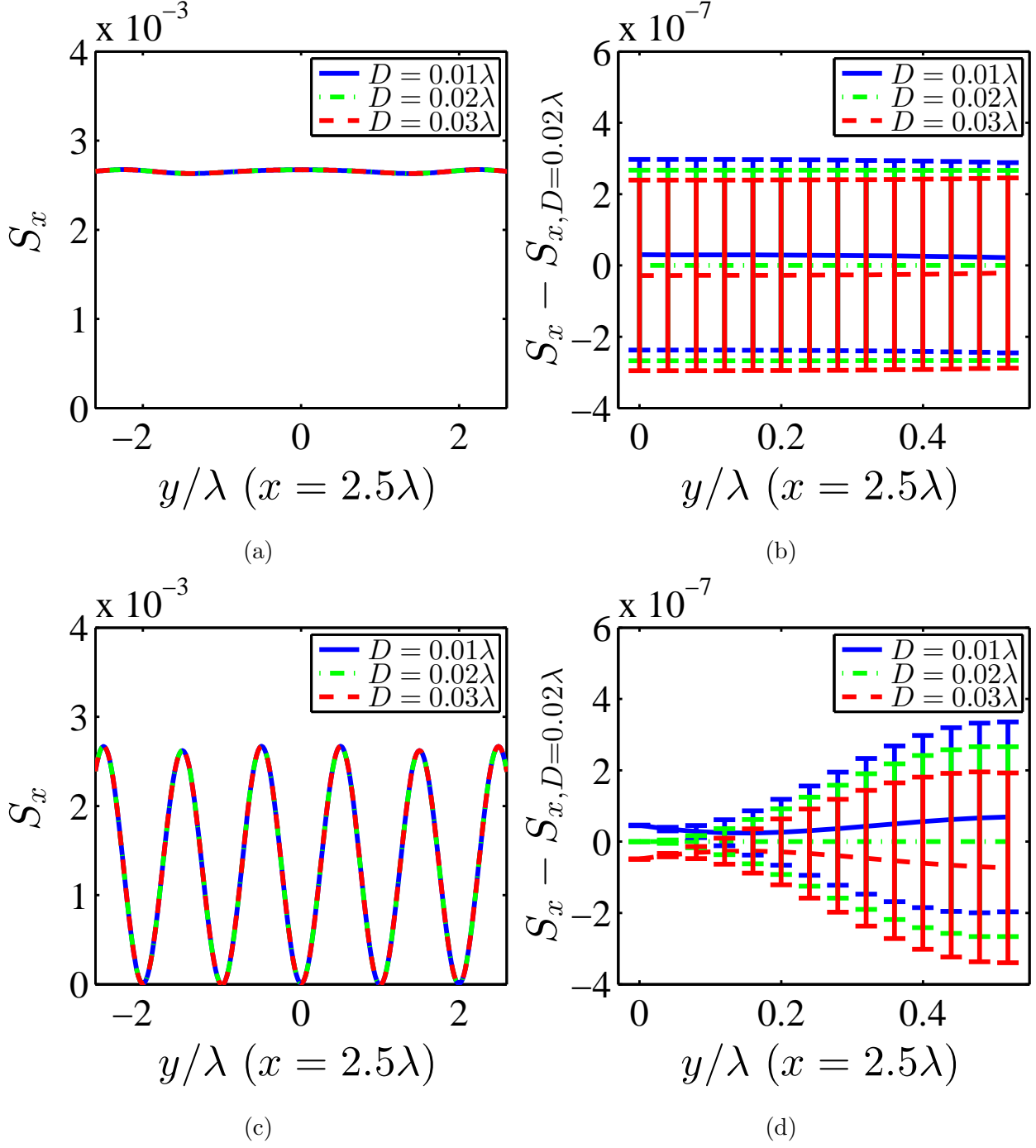
FIG. 2. Time-averaged Poynting vector in the $\hat{\mathbf{x}}$-direction, measured at s_2 for $D = 0.01\lambda$, 0.02λ, and 0.03λ, for the two $\epsilon_r = 1.5$ objects fixed at the center of the domain, $(0,0)$. The spatial coordinates refer to the geometry in Fig. 1. The PW case is shown in (a) and (b), and the SI case is shown in (c) and (d). To clearly show the error bars, corresponding to SNR=40 dB, the data plotted in (b) and (d) is for $S_x - S_{x,D=0.02\lambda}$.
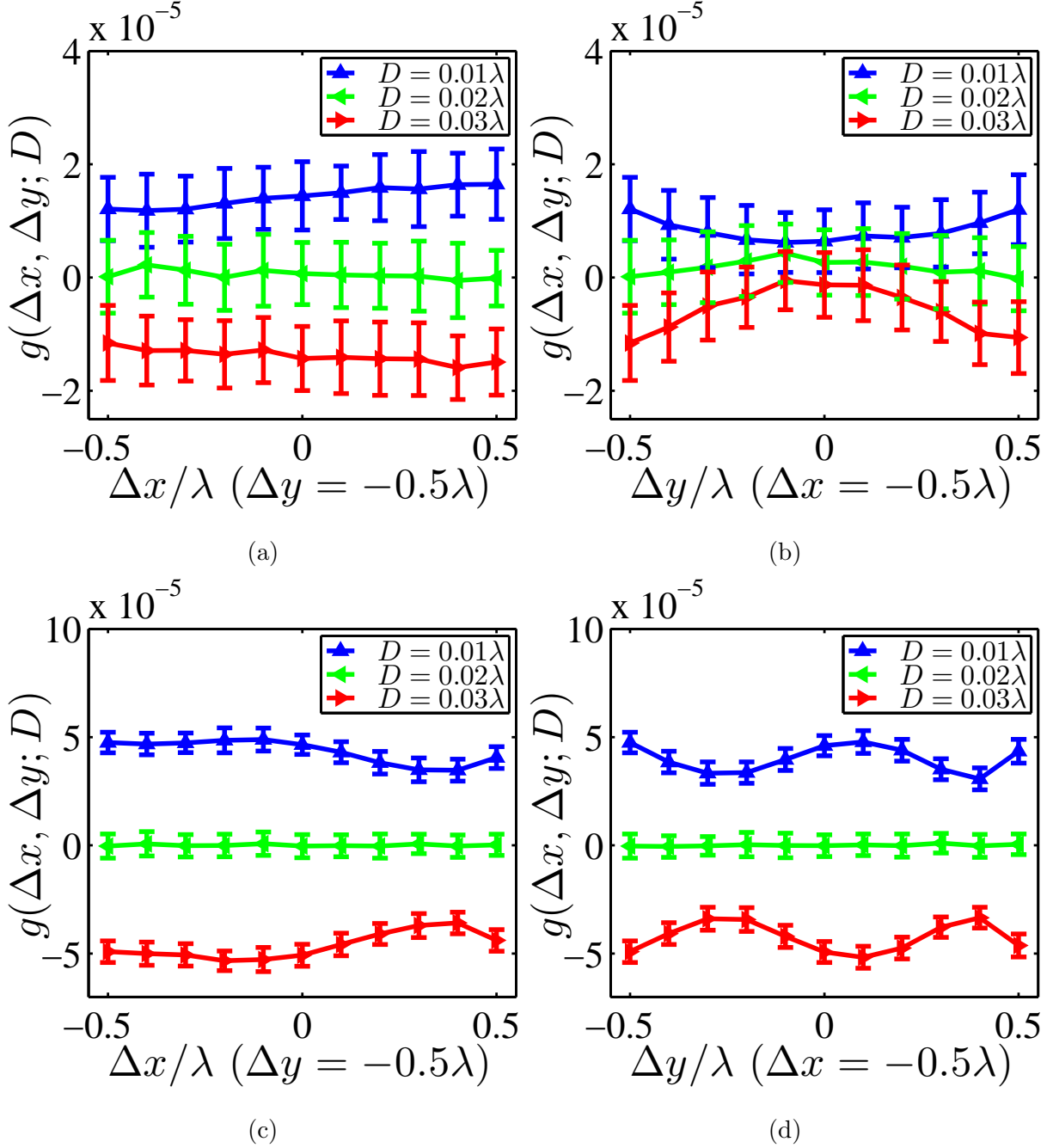
FIG. 3. Numerical values of $g(\Delta x, \Delta y; D)$ (see (5)) for the reference separation $D_0 = 0.02\lambda$ when the (two $\epsilon_r = 1.5$) scatterers are scanned along the (a) bottom and (b) left boundaries (the central region in Fig. 1(a)) for the PW case, and (c) and (d) for the SI situation, all with a SNR = 40 dB (producing the error bars, which were determined numerically with 100 Poynting vector data sets).
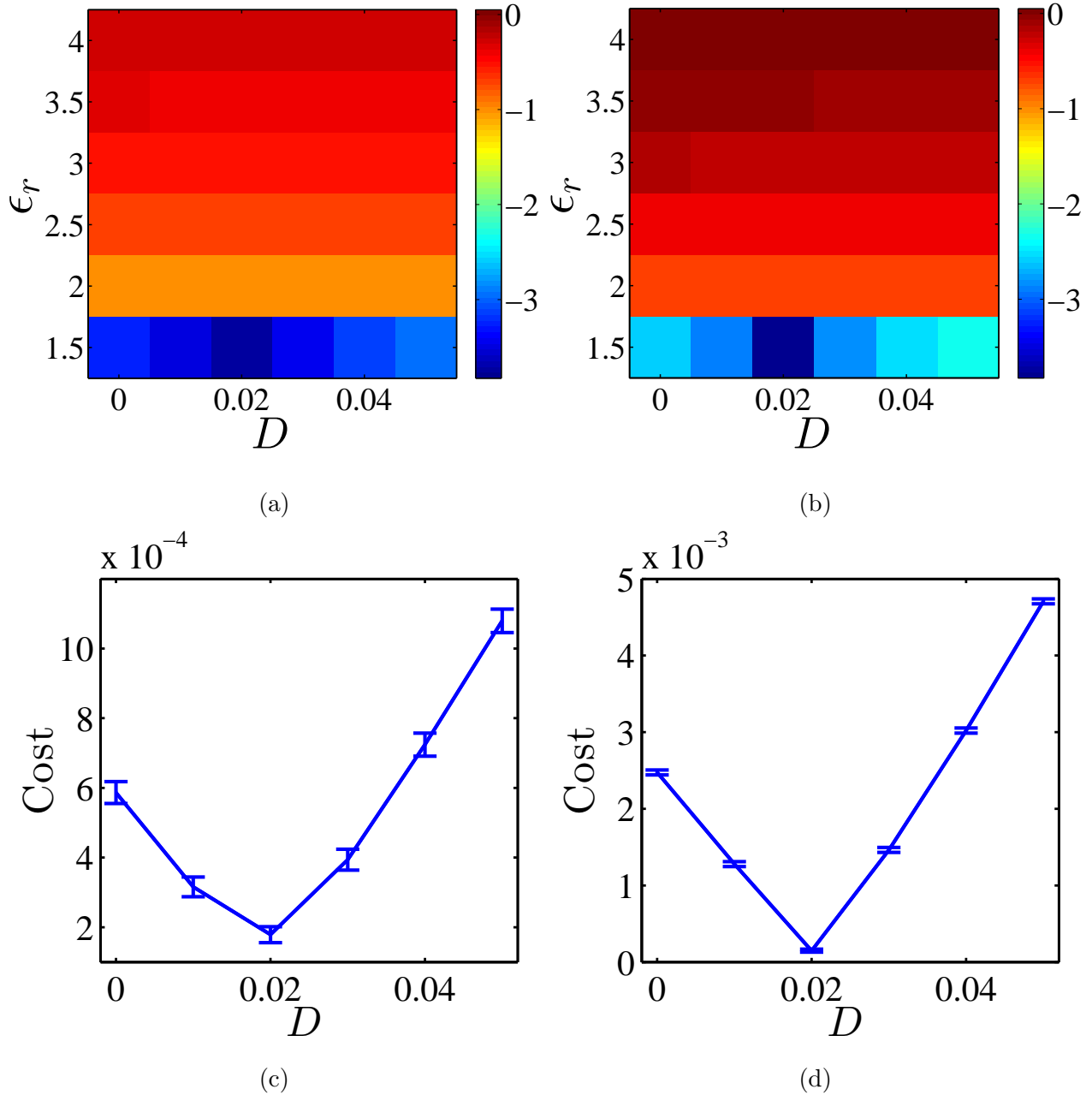
FIG. 4. Cost functions for a simulated experiment with $D^* = 0.02\lambda$ and $\epsilon_r^* = 1.5$. (a) and (b) are the decimal logarithm of the cost function for the PW and SI cases, respectively. (c) and (d) are plots of the costs for the correct value of ϵ_r for the PW and SI cases, respectively. The error bars give the standard deviation (estimated by performing the measurement 100 times with random data) assuming a SNR = 40 dB in the Poynting vector data.
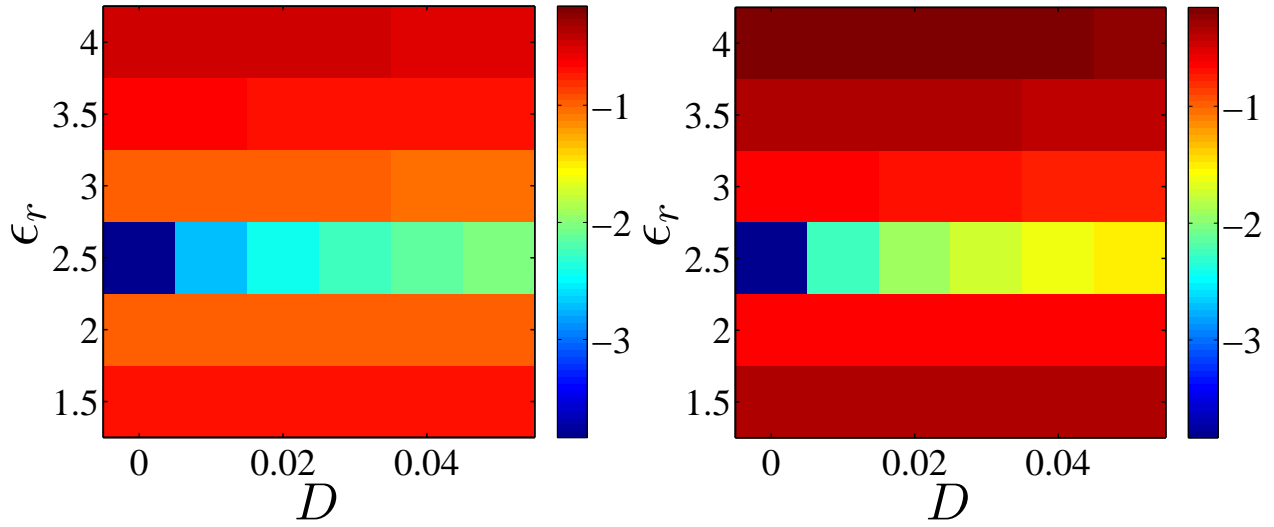
(a)

(b)
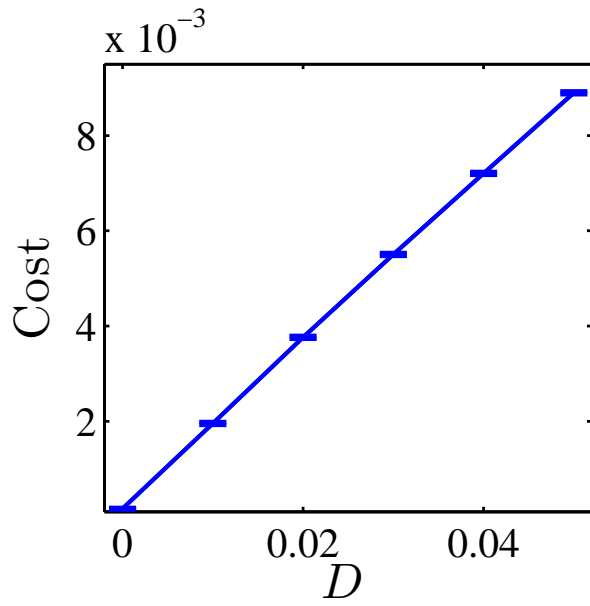
(c)
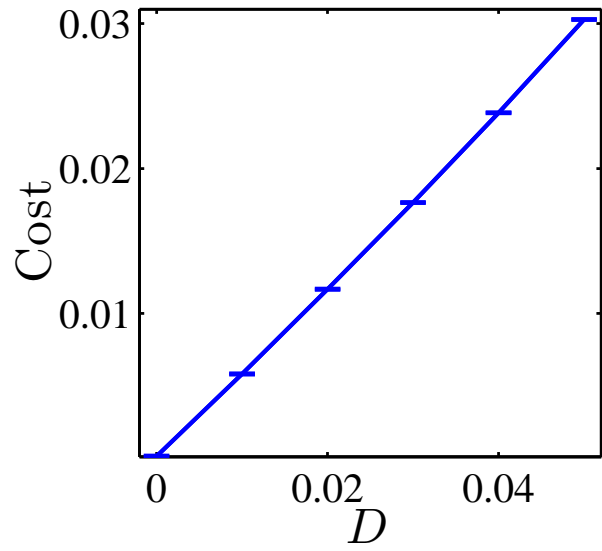
(d)

FIG. 5. Cost functions for a simulated experiment with $D^* = 0$ (a single object) and $\epsilon_r^* = 2.5$. The meaning of all sub-figures is the same as Fig. 4.

(a)

(b)

(c)
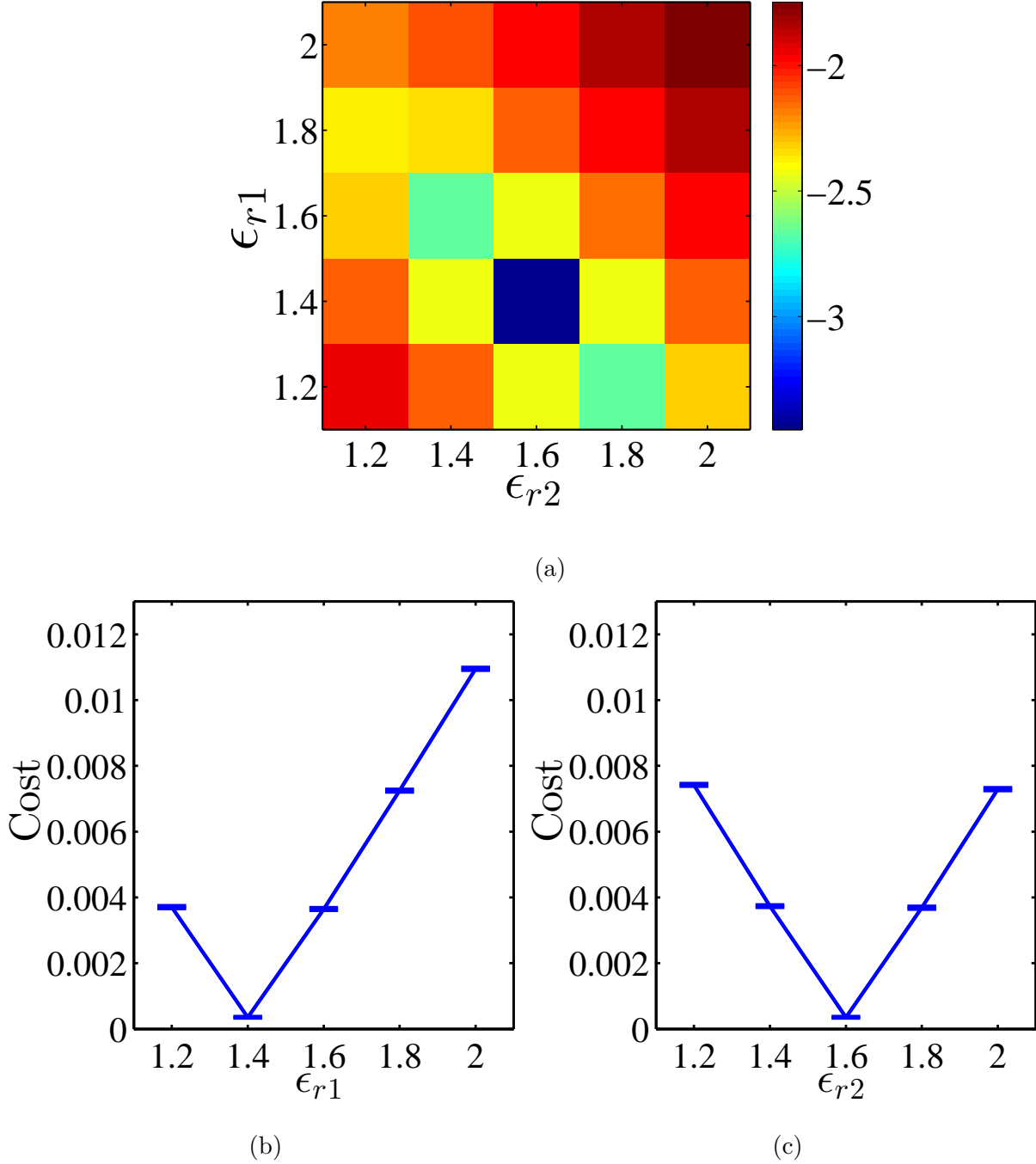
FIG. 6. Cost functions for a simulated experiment using structured illumination with the dielectric constants of the two scatters, ϵ_{r1} and ϵ_{r2}, as unknowns. (a) The discrete cost function, showing a minimum at the correct values, $\epsilon_{r1}^* = 1.4$ and $\epsilon_{r2}^* = 1.6$. (b) Cost as a function of ϵ_{r1} when $\epsilon_{r2} = \epsilon_{r2}^*$ with error bars due to detector noise. (c) Cost as a function of ϵ_{r2} when $\epsilon_{r1} = \epsilon_{r1}^*$ with the error bars.